Journal of Materials Chemistry A

ROYAL SOCIETY OF CHEMISTRY

PAPER

View Article Online
View Journal | View Issue

Check for updates

Cite this: J. Mater. Chem. A, 2025, 13, 18600

Impact of external short circuit on lithium-ion batteries: a post-mortem case study†

Shagor Chowdhury, *[a] Ana Barrera,[a] Maya Marinova,[b] Alexandre Fadel,[b] Severine Bellayer,[a] Jérôme Hosdez,[c] Clément Vandingenen,[d] Fadi Soubhie,[d] Martial Belhache,[d] Philippe Supiot[a] and Ulrich Maschke *[a]

Received 24th January 2025
Accepted 11th May 2025

DOI: 10.1039/d5ta00705d

rsc.li/materials-a

This study presents the findings of post-mortem analysis on commercial 21700 lithium-ion cells with nickel-rich NCA|graphite chemistry subjected to external short-circuiting conditions, compared to a new cell discharged to 0 V. The aim was to identify the degradation mechanisms and to assess the evolution of the battery behavior influenced by abusive external short circuit testing. A comprehensive analysis was conducted using a range of spectroscopic techniques, including X-ray computed tomography, X-ray diffraction, and scanning electron microscopy coupled with energy dispersive X-ray spectroscopy. The results of this study indicated that ESC conditions induce structural deformation in the jelly roll and enhance crack formation in both the cathode and the anode surfaces. These cracks are pivotal in comprehending the loss of active material from the cathode and its migration toward the anode. Furthermore, the active materials present in the cathode (nickel-rich NCA) and anode (graphite) have undergone modifications in their lattice property after short-circuiting, which also alters the physical properties of the separator.

1 Introduction

The increasing scarcity of fossil fuels and escalating environmental concerns are prompting numerous countries to adopt carbon neutrality policies.[1] A pivotal step in this direction is the transition from fossil fuel-based power generation to renewable energy sources such as sunlight and wind, which offer cleaner and more sustainable alternatives for the future.[2] However, the intermittent nature of renewable energy generation underscores the need for robust energy storage solutions. Lithium-ion battery (LIB) technologies are emerging as a leading solution for rechargeable energy storage due to their advantageous characteristics, including high energy densities, high power densities, and long-life cycles.[3]

LIB technology is currently utilized in a wide range of applications, including portable electronics such as laptops and smartphones, as well as electric and hybrid vehicles.[4–7] To meet the growing demand in the electric vehicle (EV) market, the production of LIBs is expanding rapidly, with annual manufacturing capacity projected to reach 2500 GW h by 2030.[8] Despite these advancements, there is significant concern regarding the battery safety issue due to the increasing number of safety incidents involving LIBs.[9,10]

These risks can be caused by a number of factors, such as overcharging, over discharging, overheating, and short circuits, leading to the degradation of the battery cell.[11,12]

Overcharging, overdischarging, and overheating can be mitigated through the implementation of a battery management system (BMS), where the critical factor lies in accurately defining voltage and temperature protection thresholds. Short circuits can be classified into two categories: internal and external.[13] An internal short circuit (ISC) occurs when the insulating separator between the positive and negative electrodes fails,[14] resulting in direct electrical contact between the electrodes.[15] This is often caused by factors such as mechanical damage, dendrite growth, or manufacturing defects (*e.g.*, microscopic metal particle contamination, tab weld defects, electrode degradation).[16–18] An ISC frequently initiates thermal runaway, posing a serious risk as it remains undetectable and unpreventable by BMS. This phenomenon has been the subject of extensive research.[19–22] In contrast, external short circuits (ESC) represent a direct connection between the positive and negative terminals on the exterior of a battery, resulting in a high current passing through the battery.[14] This phenomenon can arise from various causes, including collisions or crushing of the battery casing, failures in the seal that permit the

[a]Unité Matériaux et Transformations (UMET), UMR 8207-CNRS, University Lille, CNRS, INRAE, Centrale Lille, F-59000 Lille, France. E-mail: shagor.chowdhury@univ-lille.fr; ulrich.maschke@univ-lille.fr

[b]Institut Michel-Eugène Chevreul (IMEC) – FR 2638-CNRS, Univ. Lille, CNRS, INRAE, Centrale Lille, Univ. Artois, F-59000 Lille, France

[c]CNRS, Centrale Lille, UMR 9013 – LaMcube – Laboratoire de Mécanique, Multiphysique, Multiéchelle, University of Lille, 59000 Lille, France

[d]CRITT M2A, 62700 Bruay-la-Buissière, France

† Electronic supplementary information (ESI) available. See DOI: https://doi.org/10.1039/d5ta00705d

entrance of dust or water vapor, short-circuited sampling harnesses, damage to high-voltage system insulation, or loose connections leading to high-voltage breakdowns.

During ESC, there is a simultaneous occurrence of electrical and thermal abuse, which significantly increases the risk of large-scale thermal runaway, fire, or battery explosion.[13,23] Despite the fact that numerous research studies have been conducted to evaluate the risks associated with ESC, in batteries,[19,24] there is comparatively far less or limited knowledge acquired regarding the deterioration mechanism of the electrode materials, particularly concerning the changes at the surface and chemical levels (electronic structure, crystal structure, and morphology) occurring during such events.

It should be further highlighted that the material phenomena are expected to appear at the nanoscale level. Consequently, the employment of suitable techniques, such as scanning electron microscopy (SEM), transmission electron microscopy (TEM), and X-ray diffraction (XRD), are essential for their identification and further correlation with the structural or morphological changes that occur at the microscale.

This paper presents the characterization of commercial 21700 cylindrical cells, including new cells discharged to 0 V and cells subjected to ESC to assess the evolution of battery behavior based on aging mechanisms.

2 Materials and methods

Battery discharging and short-circuiting procedure

Commercial 21700-type Li-ion batteries (Model: Samsung® INR21700-53G) were utilized in the testing process. The batteries were discharged to 0 V using an electronic load. Electrical abuse tests consist of performing an external short circuit (across the cell terminals) following a procedure similar to that of the IEC 62620-2 standard (see Fig. S1†). Prior to the constant current (CC) procedure, the cells underwent a specific charge/discharge cycle to ensure an identical state of charge (SOC) level of 100%.

Each cell was tested individually and positioned in a cylindrical cell holder within the abuse bench. The short circuit was facilitated by a power contactor. The assembly's resistance was measured at 1.3 mΩ. The cell was equipped with three thermocouples, as illustrated in Fig. S1.† Initial tests were conducted at a temperature of 20 °C, and subsequently, the temperature was increased. The duration of the short circuit is dependent on the opening of the Current Interrupt Device (CID).

Materials characterization

In the present study, the characterization of materials and components of the cell was conducted using various advanced techniques. It is noteworthy that the analysis was conducted on a total of five lithium-ion cells, of which two were in pristine condition and three had undergone ESC. To ensure reproducibility and representativeness, a uniform procedure was employed for all cells. The cells were opened in an argon-filled glove box, and sampling was carried out across all layers of each cell involved multiple regions of the electrodes and separator. Samples were obtained at intervals of approximately 10 centimeters along the length of the layers.

A JEOL JSM-7800F LV SEM, equipped with an energy dispersive X-ray (EDX) spectrometer, was used to analyze the surface morphologies and perform chemical composition analysis (weight percentage). These investigations were performed on carbon-coated samples in a high vacuum mode at an accelerating voltage of 20 kV. To perform elemental analysis, a Cameca SX100 electron probe microanalyzer (EPMA) was utilized on carbon-coated samples. The back-scattered electron images were carried out at 15 kV, 15 nA, and full detection spectra were carried out at 15 kV, 15 nA using PC2, LiF, LPET, and TAP analyzer crystals. The measurement of crack sizes was conducted by employing the Fiji distribution of the open-source software ImageJ.

A Thermo-Fisher Scientific TITAN Themis (300 keV) equipped with a high brightness Schottky field emission source and a Wien-type monochromator was utilized to obtain high angle annular dark field (HAADF) images in the scanning TEM (STEM) mode on the focused ion beam (FIB) extracted lamellae. The HAADF imaging was performed with a semi-convergence angle of 20 mrad, a probe size of approximately 0.1 nm, and a beam current of 100 pA. The camera length was selected to provide collection angles for the HAADF detector between 55 mrad and 200 mrad. The bright field images and selected area electron diffraction patterns were obtained in broad parallel beam transmission electron mode.

Contact angle measurements were performed using a Krüss DSA10 goniometer. Raman spectroscopy was carried out using a homemade system built with a Jobin-Yvon Triax 180 spectrometer with a grating of 1800 lines/mm, a Horiba Synapse CCD camera that runs with LabSpec software. Differential Scanning Calorimetry (DSC) analysis was performed using a PerkinElmer DSC 8000 model at heating and cooling rates of 10 °C min^{-1}, under continuous nitrogen flow. Samples with masses ranging from 6 to 12 mg were analyzed using a temperature ramp of 10 °C min^{-1} between −70 and 100 °C. To ensure the reliability of the results, three heating and cooling cycles were conducted. Fourier-transform infrared (FTIR) spectroscopy was performed using a Frontier spectrophotometer (PerkinElmer, Waltham, MA, USA) to examine infrared absorption characteristics. X-ray fluorescence (XRF) spectrometry (Bruker S2 Ranger) was employed to determine the elemental composition. The crystalline structure of the electrode materials was characterized using a Rigaku Miniflex 600 XRD (Rigaku, Tokyo, Japan) equipped at 40 kV and 15 mA with Cu Kα radiation (λ = 1.5406 Å Goniometer Miniflex 300/600). The samples were scanned from 2° to 80° (2θ) using a step scan of 0.02° and a counting time per step of 0.5 s. Phase identification and peak indexing were carried out using DIFFRAC.EVA V5.2 software. The lattice parameters utilized in this study correspond to those provided by the 2025 version of the Powder Diffraction File (PDF) database, which is integrated into DIFFRAC.EVA and employed during the matching of the experimental diffractogram with reference patterns.

X-ray computed tomography (XCT) was performed using a Microtomograph ULTRATOM to obtain detailed cross-sectional images of the cell structure.[25] In this study, a 160 kV acceleration voltage was utilized alongside a filament current of 200 mA. The source-to-object distance was set at 43.19 mm, while the source-to-detector distance was 274.23 mm. Helicoil tomography with five turns was employed for profile acquisition, and the tomographic data were reconstructed using a filtered back-projection algorithm, executed with the X-act software. Elemental analyses were performed using an optical emission spectrometer (ICP-OES, Agilent 5100 dual targeted).

3 Results and discussion

Cell inspection using X-ray computed tomography

Prior to disassembly, X-ray computed tomography (XCT) was conducted to capture non-invasive images of the cell's internal structure (Fig. 1) and to evaluate how external short-circuit events influence its full internal architecture. Generally, elements with high atomic numbers are displayed with higher gray scale values compared to elements with low atomic numbers.[26]

Computed tomography scans of the pristine cell (Fig. 1A) revealed a structure comprising 25 electrode double layers with an average thickness of approximately 254.5 μm. The scans further revealed the absence of significant deformations in the structure of the jelly roll, which is composed of a cathode, an anode, and a separator wound together.[27] In contrast, the ESC cell (Fig. 1B) displayed pronounced buckling of the jelly roll toward the rotational axis of the cylinder, leading to kinks in the anode, cathode, and separator, primarily in the inner 14 layers of the cell with similar average thickness of electrode double layers (≈256 μm). The initiation of this phenomenon was predominantly observed in proximity to the current collector. This behavior has been previously reported by Waldmann *et al.*,[28] and it is attributed to the higher specific resistance of aluminum, which results in elevated temperatures due to ohmic heating of the current collector and tabs.

Disassembly of the battery cells

A post-mortem analysis was performed to assess the structural damage. The cells were meticulously disassembled in an argon-rich glovebox within a controlled environment (O_2 < 0.1 ppm, H_2O < 0.1 ppm). During retrieval, the positive electrodes, negative electrodes, and separator were meticulously isolated to prevent cross-contamination. After opening the cell in the glovebox, immediate visual inspection of the cell components was performed. The isolation process for electrodes and the separator of the pristine cell discharged to 0 V (Fig. 2A) was easier compared to the cell exposed to ESC conditions (Fig. 2B). In the latter case, both the positive and negative electrode sheets were firmly adhered to the separator. Furthermore, the chemical components were observed to be detached from the anode and deposited on the separator. In both conditions, the separator was found to be dry, and the black stains on the separator are attributed to negative electrode particles, caused either by adherence or dismounting process.[29]

The adhesion in ESC cells is likely associated with thermal melting and electrolyte decomposition. As demonstrated in Fig. S2 of the ESI,† during the ESC operation, there was a sudden increase in current to over 200 A, accompanied by a corresponding decrease in voltage (red curve). The current that flows through the cell generates heat at a rate of over 100 °C in a brief period of time. As has been previously demonstrated, the electrolyte undergoes decomposition at elevated temperatures.[14] At temperatures above 90 °C, the breakdown of the solid electrolyte interphase (SEI) on the anode becomes exothermic, thereby further increasing the temperature. This decomposition may yield a variety of organic and inorganic compounds that could function as adhesive agents between cell components.

Analysis of the cathode surfaces

The nature and the elemental composition of the cathode surfaces were analyzed using both inductively coupled plasma (ICP-OES) spectrometry and X-ray fluorescence (XRF) spectrometry. Both techniques yielded consistent results, indicating

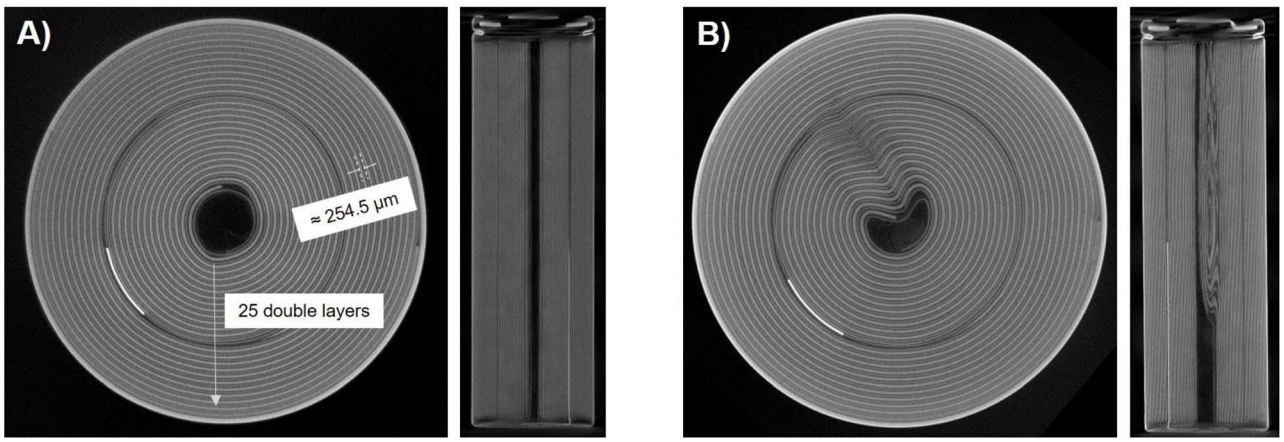

Fig. 1 CT images showing the cross-sectional and longitudinal views of a commercial 21700 cell (A) pristine cell discharged to 0 V and (B) cell subjected to ESC conditions.

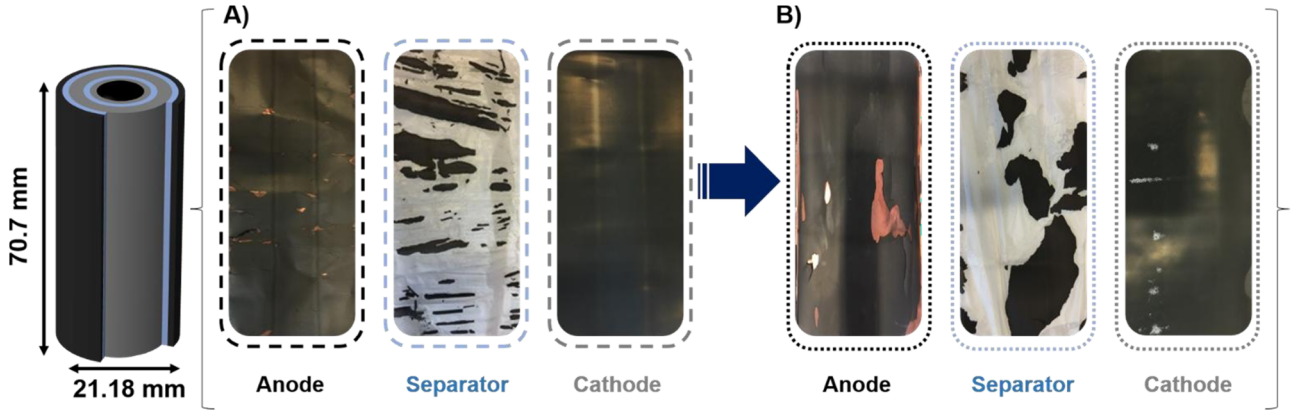

Fig. 2 Digital micrographs of the isolated electrodes and separators of (A) pristine cell discharged to 0 V and (B) cell subjected to ESC conditions.

that the positive electrode in the pristine cell discharged to 0 V (Fig. S3†) and in the cell subjected to external short-circuit (ESC) conditions (Fig. S4†) is composed of a nickel-rich NCA (nickel–cobalt–aluminium) material with the general formula $LiNi_{1-x-y}Co_xAl_yO_2$. The disparities in elemental composition between the pristine and ESC NCA cathodes can be attributed to thermally induced degradation and element redistribution resulting from the short-circuit event. The observed decrease in Ni content and the increase in Al content suggest surface reconstruction and possible Al migration from the current collector under high-temperature conditions. The presence of Ca (0.2%) and Fe (0.16%) in the ESC sample suggests the possibility of contamination from internal components, such as electrolyte additives, separators, and casings, that have become mobilized during thermal stress. These compositional shifts are consistent with localized decomposition and interfacial reactions characteristic of thermal abuse scenarios.

The morphological structures of the electrodes were investigated by means of SEM analysis to visualize the structural changes induced by ESC as illustrated in Fig. 3. Cathodes consist of nearly characteristic round agglomerates of NCA with an apparent bimodal size distribution which are built up of smaller primary NCA particles. In the electrode retrieved from the pristine cell discharged to 0 V (Fig. 3A), the large circular agglomerates within the selected region have an average diameter of 15.36 μm and an average area of 211 μm^2 (Fig. S5†). In contrast, the electrode from the cell subjected to ESC conditions (Fig. 3B) demonstrates an increase in agglomerate

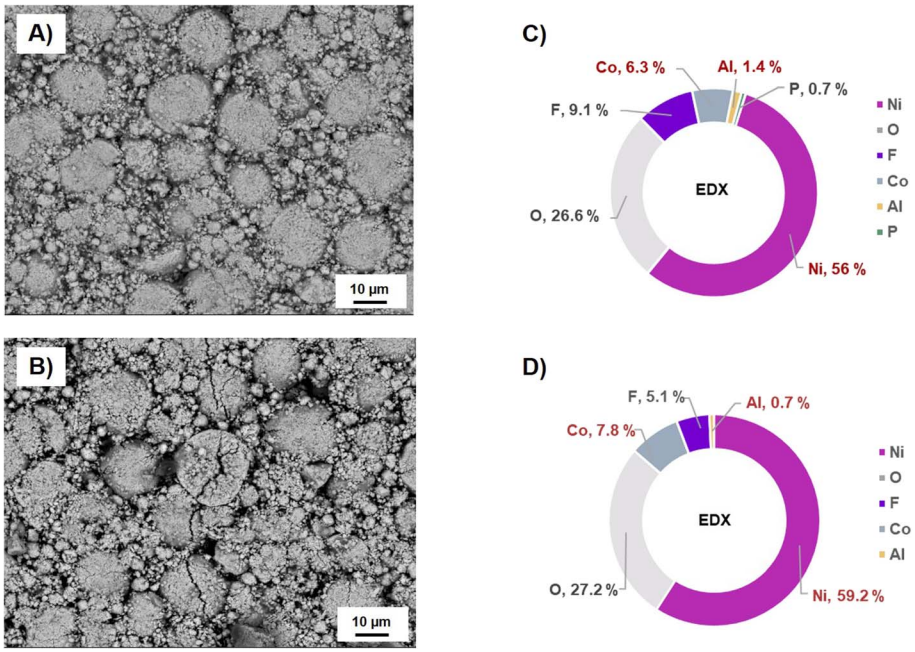

Fig. 3 SEM micrographs (backscattered images) of the surface of the positive electrodes retrieved from (A) pristine cell discharged to 0 V and (B) cell subjected to ESC conditions. EDX analysis (weight percentage) of the chemical composition of the negative electrodes retrieved from (C) pristine cell discharged to 0 V and (D) cell subjected to ESC conditions.

size, exhibiting an average diameter of 17 μm and an average area of 262 μm^2 (Fig. S6†). Importantly, the NCA-based electrode from the short-circuited cell exhibits significantly more pronounced cracking features compared to the pristine cell electrode, where only few cracks were observed. These cracks appear to lead to induce the fragmentation of agglomerates into smaller, irregularly shaped agglomerates or even into individual primary particles, as revealed by TEM analysis. The resulting particles, measuring less than a micrometer in size, have been found to exhibit nano-inclusion (Fig. S7†). The agglomerates observed in Fig. S7† were identified as secondary spherical particles based on size and morphology, as determined using ImageJ software. The diameter of primary NCA particles is typically less than 1 μm, while the secondary particles observed here exceed several micrometers. These larger structures are the result of the agglomeration of primary crystallites, and they have been shown to affect performance, with rate capability being inversely correlated to particle size. Under ESC conditions, structural variations such as cracking within secondary particles may occur, contributing to mechanical and electrochemical degradation.

The EDX maps (Fig. S8†) and the EPMA equipped with wavelength dispersive X-ray spectrometer (WDS) analysis (Fig. S9†) of the electrodes from both cells revealed a homogeneous distribution of Ni and Co, accompanied by a less uniform distribution of Al. For clarity, the scale bars and image dimensions of the EDX maps in Fig. S8† have been standardized to allow for better qualitative comparison. It should be noted that EDX mapping is semi-quantitative, and direct comparison of color-coded areas is not suitable for accurate elemental quantification.

Complementary point analysis was used to assess elemental ratios more reliably.

This observation serves to further substantiate the composition and nature of the nickel-rich NCA electrodes, which are comprised of the elements present in the following proportions: Ni > Co > Al (Fig. 3C, D and S9†).

Crack formation was observed within the NCA secondary particles in the post-mortem analysis of the short-circuited cells. Given the absence of electrochemical cycling, it can be excluded that electrochemical stress, typically associated with repeated lithium intercalation/deintercalation, is the primary cause. However, during the short-circuit operation, a significant increase in temperature and discernible gas generation were observed (Fig. S2 and S10†). These observations imply that thermal and mechanical stresses are likely contributors to the observed particle cracking. Localized heating has been shown to induce thermal expansion mismatches within the electrode material, while gas evolution may result in increased internal pressure.[30,31] These phenomena can promote intergranular and intragranular crack propagation. Despite the absence of temperature-dependent imaging in the present study, the observed morphological features are consistent with degradation mechanisms driven by thermal and mechanical stress.

While no electrochemical cycling or impedance measurements were performed in this study, the observed morphological changes, such as agglomerate cracking and particle fragmentation, are widely recognized as detrimental to battery performance. These structural defects can increase internal resistance, promote transition metal dissolution, and reduce active material utilization.[32] Ultimately, these defects contribute to capacity fading and impedance rise during cycling. Furthermore, such damage may compromise the mechanical integrity of the electrode, thereby elevating the risk of safety-related events under abusive conditions.

To gain further insights, X-ray diffraction (XRD) analysis was performed on the cathode surfaces (Fig. 4). The XRD patterns indicated that the NCA material in both electrodes exhibited a layered hexagonal α-$NaFeO_2$-type structure belonging to the $R\bar{3}m$ space group.[33,34] The extent of the observed structural expansion was quantitatively assessed by means of identification of phases of the XRD data. This analysis revealed a substantial increase in the lattice parameter *c*, from 14.1868 Å in the pristine cathode to 14.463 Å in the electrode that had been subjected to ESC (Fig. S11†). Conversely, the lattice parameter *a* exhibited a slight decrease from 2.8709 Å to 2.822 Å, suggesting anisotropic lattice distortion under short-circuit conditions. The *c*-axis expansion was further supported by the increase in $d_{(003)}$ spacing, as observed in SAED patterns and HAADF-STEM images, which showed a change from 4.67 Å in the pristine cathode to 4.72 Å in the ESC sample (Fig. S12 and S13†). These findings are consistent with previous reports linking thermal and mechanical stress to structural distortion in layered oxide cathodes.

The narrow profile of the diffraction lines in the cathode surface of the pristine cell discharged to 0 V indicates

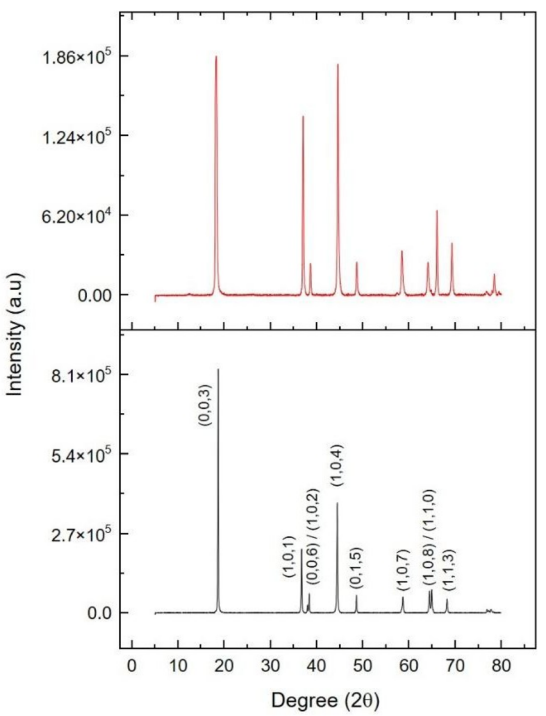

Fig. 4 XRD patterns of the cathode surfaces retrieved from pristine cell discharged to 0 V (black) and from the cell subjected to ESC conditions (red).

a homogeneous distribution of cations within the structure.[35] Furthermore, the distinct splitting of the (108)/(110) and (006)/(102) peaks suggests a well-ordered layer structure that facilitates the lithium transport in lithium-ion battery cells.[36,37]

However, the diffraction peaks corresponding to the positive electrode from the ESC affected cell exhibited slight broadening and reduced resolution, with the absence of splitting of the (006)/(102) peaks. This finding indicates reduced crystallinity and suggests signs of deterioration in the NCA material.[38] Furthermore, the (003) crystal plane diffraction peak shifts slightly toward lower angles, suggesting an expansion in the cell parameters.[34] Another notable effect of short-circuiting is the increase in the degree of cation disorder, as evidenced by the decrease in the intensity ratio $I_{(003)}/I_{(104)}$ from 2.2 to 1.03. This phenomenon can be attributed to the partial migration of Ni^{2+} ions in Li^{+} sites due to the low transition barrier. The Ni^{2+}/Li^{+} cation mixing effects have been thoroughly documented in layered NCA cathode materials, particularly those with elevated nickel content. It has been demonstrated that Ni^{2+} and Li^{+} possess comparable ionic radii (0.69 and 0.76 Å, respectively). This similarity in radii suggests the potential for Ni^{2+} to migrate into the lithium layers, resulting in partial occupation of Li^{+} sites. This cation disorder disrupts the layered structure, thereby reducing the number of accessible pathways for lithium-ion diffusion. Consequently, this phenomenon impedes Li^{+} mobility, increases polarization, and contributes to reduced rate capability.

In addition to impeding Li^{+} transport, Ni^{2+}/Li^{+} mixing has been shown to reduce the initial discharge capacity by decreasing the amount of reversibly extractable lithium. It has been demonstrated that this phenomenon is associated with an increase in interfacial and bulk impedance, which has a deleterious effect on cycling performance.[39,40] In the context of high-voltage operation, this mixing has the potential to enhance structural degradation, including phase transitions and microcracking. This, in turn, can contribute to long-term capacity fading.

Analysis of the anode surfaces

A thorough investigation was conducted into the anode electrodes to ascertain the effect of ESC conditions on them. Initially, the chemical composition was determined using XRF (Fig. S14†). The anode from the pristine cell discharged to 0 V primarily contained C, P, and Si. In contrast, the anode from the ESC-affected cell exhibited the presence of C, Si, P, Ni, and Co. The presence of C and Si corresponds to the active anode materials, while P is most likely derived from the electrolyte. The presence of Ni and Co in the ESC-affected anode suggests their migration from the cathode surface, which might be due to the dissolution of transition metals and their subsequent deposition into the anode.[41] Consequently, this process has the potential to reduce the energy density of the cathode.[42] To shed light on the transition metal deposition on the anode, comprehensive SEM/EDX analyses were performed. Morphologically, the anode surface retrieved from the pristine cell discharged to 0 V exhibited a more uniform appearance compared to the anode from the cell subjected to ESC conditions (Fig. 5A and B). In the latter, cracks with granular texture, with small and blurred regions, and scattered white particles were visible across the electrode surface (indicated by red arrow in Fig. 5B). The chemical composition of both electrodes was examined using EDX mapping, which revealed a homogeneous distribution of P and O, as well as an irregular distribution of Si

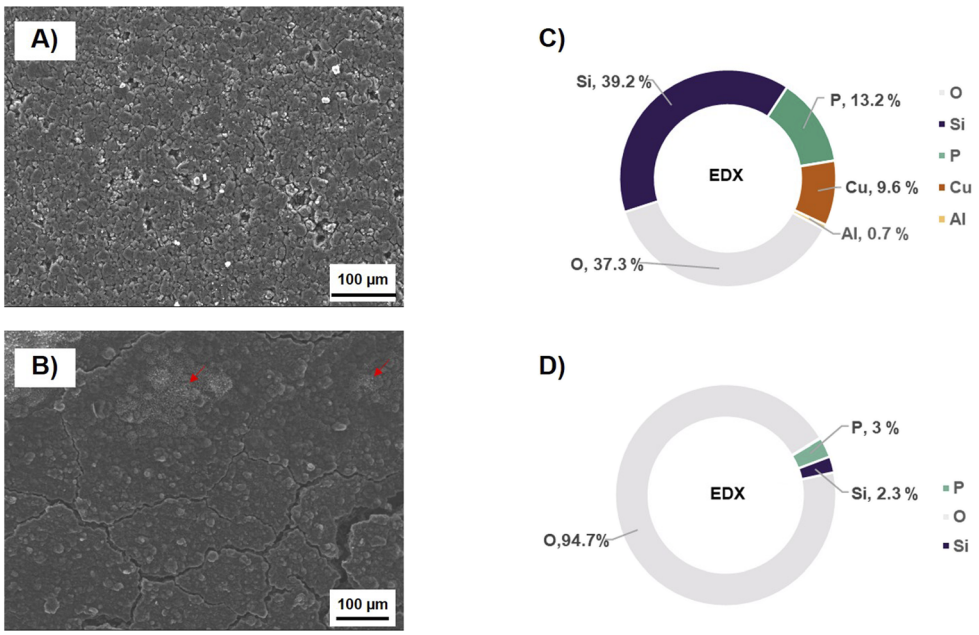

Fig. 5 SEM micrographs (secondary electron image) of the anode surface retrieved from (A) pristine cell discharged to 0 V (B) cell subjected to ESC conditions. EDX analysis (weight percentage) of the chemical composition of the anode surface retrieved from (C) pristine cell discharged to 0 V and (D) cell subjected to ESC conditions.

(see Fig. 5C, D and S15†). It is noteworthy that the carbon content could not be measured due to the use of a carbon coating on the sample, which resulted in a significant percentage of oxygen.

In the endeavor to locate the deposited transition metals, it was ascertained that their identification was more straightforward in the anode electrodes retrieved from the cell subjected to ESC conditions. These transition metals appeared to be embedded within the graphite structure (Fig. 6A) and were predominantly observed in areas exhibiting cracking features (Fig. 6B) or surface morphology variations (Fig. 6C). To strengthen the interpretation of the correlation between morphological degradation and transition metal deposition, several additional regions of the anode surface were examined. Transition metals such as Ni and Mn were also detected in regions without visible cracks or surface irregularities, although their signal was generally weaker and more difficult to locate. In contrast, regions exhibiting distinct morphological features (*e.g.*, cracks or blurred texture) consistently showed more pronounced signals of deposited transition metals, facilitating their identification.

In the case of the pristine anode, transition metal signals were scarce and insufficient for mapping analysis. Therefore, elemental identification was performed using point spectra mode rather than EDX mapping, as presented in Fig. S16.†

This phenomenon could be attributed to calendar aging, which is a consequence of the thermodynamic instability of the materials.[43,44] The validity of these findings is further substantiated by EPMA spectroscopic analysis (Fig. S17†).

In order to verify the nature of the anode material and further characterize its properties, XRD was performed on the negative electrodes. The XRD spectra revealed the presence of a characteristic peak of graphite at $2\theta \approx 26°$, as observed in the anode material extracted from the pristine cell discharged to 0 V (Fig. S18†). The observed layered structure with a hexagonal space group ($P6_3/mmc$) (Fig. S19†) is attributed to the sp^2 hybridization of the carbon atoms, which is a characteristic feature of carbon-based materials.[45,46] In this structure, the carbon atoms form strong in-plane covalent bonds, creating a hexagonal lattice, while the out-of-plane interactions are weaker, allowing for the formation of distinct layers held together by van der Waals forces.

In comparison, the diffraction peaks from the anode material retrieved from the cell subjected to ESC conditions were broader with lesser intensity (Fig. S18†). This broadening indicates a reduction in crystallinity, the formation of defects, and a decrease in crystallite size.[47,48] This finding was further confirmed by calculating the crystallite size from the graphite (002) peak at $2\theta \approx 26°$, which decreased from 38 nm for the pristine cell discharged to 0 V to 27 nm for the ESC-affected cell. The formation of defects has been studied by Raman spectroscopy (Fig. 7). In general, the Raman spectrum of a graphite consists of the G-band (which represents the E_{2g} mode of pristine sp^2 carbon atoms), the D-band (which appears in the case of a defective lattice) and the 2D-band (which is present independently of lattice defects).[49] The ratio of the D-band to G-band integral is frequently used to measure the degree of lattice disorder and defects.[50] In this study, the I_D/I_G ratio increased from 0.41 for the pristine cell discharged to 0 V to 0.52 for the cell subjected to ESC conditions, confirming the development of edges and defects upon short circuiting process. A higher density of defects resulting from the short-circuiting process was evidenced by the SAED pattern and BF-TEM images, as shown by the presence of pronounced streaks (Fig. S20 and S21†).

Analysis of the separator

Chemical analysis was performed using FTIR technique on separator residues from pristine and ESC cells (Fig. S22†). The

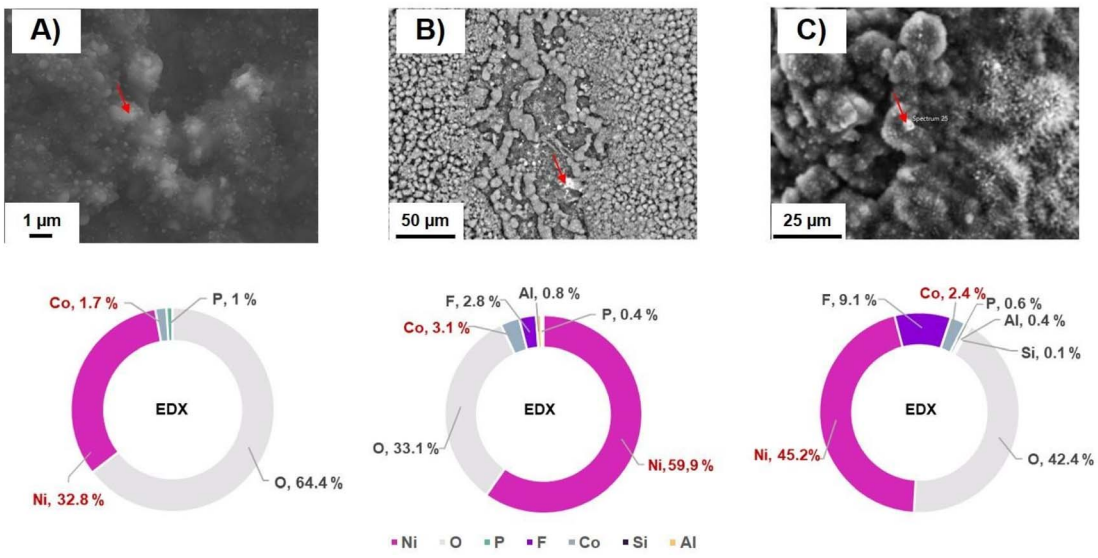

Fig. 6 SEM micrographs ((A and C) secondary electron image – (B) backscattered image) at different regions and corresponding chemical composition analysis (weight percentage) below the micrographs of the particle marked by a red arrow on the anode surface retrieved from the cell subjected to ESC conditions.

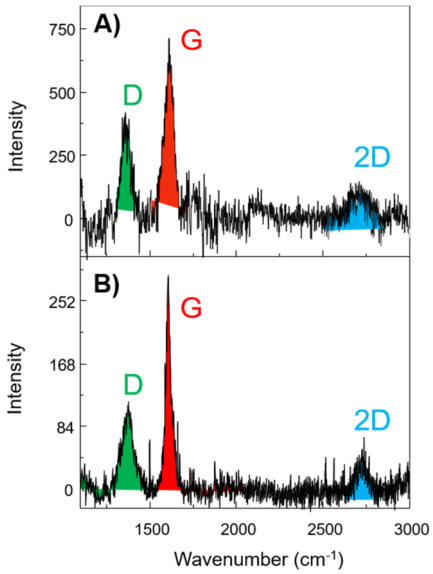

Fig. 7 Raman spectra of the anode surfaces retrieved from (A) the cell subjected to ESC conditions and (B) pristine cell discharged to 0 V.

IR spectrum of the separator isolated from the pristine cell discharged to 0 V showed four characteristic peaks of polyethylene (PE) at 719 cm^{-1} (C–H bending), 1472 cm^{-1} (C–H bending), 2849 cm^{-1} (C–H stretching), and 2918 cm^{-1} (C–H stretching). In the ESC sample, these peaks persist but with reduced intensity and resolution, indicating partial degradation of the polymer chains. However, their presence indicates that the hydrocarbon backbone remains largely intact.

In the 2000–1500 cm^{-1} region, two additional peaks were observed in the pristine separator: the vibrational band at ~1730 cm^{-1} corresponding to C=O stretching of free (uncoordinated) carbonate solvents such as EC, DMC, EMC, and DEC; the band at ~1620–1600 cm^{-1} attributed to lithium-coordinated carbonyl stretching, where interaction with Li^+ weakens the C=O bond and shifts the peak to lower wavenumbers. In addition, a distinct peak at 840 cm^{-1} was also observed in the pristine separator and is attributed to the P–F stretching vibration in $LiPF_6$. These peaks are absent in the ESC sample, indicating that liquid electrolyte components were decomposed or desorbed during the thermal stress induced by the ESC.

The DSC thermograms (Fig. S23†) display endothermic peaks at approximately 140 °C and exothermic peaks at 120 °C. These thermal events are consistent with the melting and crystallization behavior of PE, suggesting its possible presence in the analyzed sample. In particular, the left side of Fig. S23† presents the first heating and cooling cycles of pristine and ESC samples, whereas the right side of Fig. S23† shows the second heating and cooling cycles.

During the first heating cycle (left side of Fig. S23†), the ESC sample exhibits a thermal profile that differs noticeably from that of the pristine sample. This deviation is likely due to structural modifications resulting from the short-circuit, which may have altered the separator's morphology and microstructure. Partial degradation of the SEI may have occurred during the short circuit, which might effected the separator and thus to minor exothermic peaks between 80 and 120 °C, as seen in the DSC curve. Additionally, the formation of lithium metal dendrites in the ESC cell could have triggered further reactions with the electrolyte upon heating, producing extra exothermic signals absent in the pristine sample. While both separators show a melting peak, typically observed between 120 and 150 °C in polymer-based separators, their profiles differ, likely due to the thermal and electrochemical history of the ESC sample.

In the second heating cycle (right side of Fig. S23†), the thermal behavior of both samples becomes nearly identical. This convergence suggests that both separators underwent complete melting and recrystallization during the first cycle, which effectively reset their crystalline structures. Reactive or volatile components such as residual electrolyte, lithium dendrites, and decomposition products appear to have been consumed or removed during the initial thermal treatment. As a result, the material loses any "thermal memory" of prior mechanical or thermal stress, and both samples return to a similar thermodynamic state.

However, SEM imaging of the separator revealed two distinct surface morphologies: the side facing the cathode was enriched with aluminum (Fig. S24†), while the side facing the anode was enriched with carbon-coated PE (Fig. S25†). On the other hand, the side facing the anode corresponds to the aluminum current collector. Although this surface is coated with a thin carbon/PE layer, its contribution could not be quantified due to the high absorption factor and the exclusion of the carbon coating from the weight percentage calculations (Fig. S25†).

In accordance with the observations made for the electrodes previously discussed, the separator extracted from the cell subjected to ESC conditions frequently exhibited the presence of Ni and Co. Conversely, these elements were scarcely detected in the separator taken from the pristine cell discharged to 0 V (Fig. S26 and S27†).

While the precise mechanism responsible for Ni and Co deposition could not be directly identified within the scope of this study, a plausible explanation involves the dissolution of transition metals from the NCA cathode, followed by their migration through the electrolyte and subsequent deposition onto the separator. This process may be exacerbated under ESC conditions due to localized heating, electrolyte decomposition, or sharp potential gradients that accelerate metal dissolution and transport. However, given the lack of electrochemical cycling and the post-mortem nature of our analysis, it is not possible to definitively determine the pathway or kinetics of this phenomenon.

In addition to compositional changes, these observations point to a broader impact on the physical properties of the separator. Following the short-circuiting event, an increase in the average surface roughness (R_a) was observed on both sides of the separator (Fig. S28 and S29†). Moreover, the wettability of the separator material was significantly altered. In the pristine cell, the side of the separator facing the anode exhibited hydrophobic behavior, while the cathode-facing side was hydrophilic and allowed complete spreading of water (Fig. S30†). In contrast, for the separator retrieved from the ESC-

affected cell, the anode-facing side became less hydrophobic, and the cathode-facing side displayed reduced hydrophilicity.

These morphological and surface property changes further support the central focus of this study, which is the post-mortem analysis of NCA-based electrodes and separators from short-circuited cells, with the aim of identifying morphological and chemical signatures associated with ESC. Despite the absence of electrochemical cycling, alterations in the separator's wettability were clearly discerned during characterization. While these findings suggest possible interactions between electrolyte components and separator surface chemistry, a comprehensive analysis of how wettability relates to ionic conductivity and thermal behavior was beyond the scope of the present investigation.

4 Conclusions

This study conducted post-mortem analyses of commercial 21700 lithium-ion batteries (LIBs) subjected to external short-circuit (ESC) conditions and compared them to a new battery discharged to 0 V. The objective was to investigate the surface deterioration and modifications in the cathode, anode, and the separator. The ESC condition was found to induce structural deformation in the jelly roll and promote the formation of cracks on both the cathode and the anode surface. These cracks appeared to play a vital role in the loss of active material from the cathode surface and its subsequent migration to the anode. Additionally, the active materials present in the cathode (nickel-rich NCA) and anode (graphite) underwent modifications in their lattice properties due to short-circuiting, which also impacted the physical characteristics of the separator.

In contrast to previous studies focusing on thermal and electrical behavior of cells under abuse conditions including ISC and ESC, this work employs a multidisciplinary approach (X-Ray computed tomography, SEM/EDX, TEM, XRD, FTIR, Raman, TGA, DSC, contact angle measurements, …) to reveal novel microstructural degradation processes as mentioned before. The findings of this study offer novel insights into previously under-documented failure pathways.

In order to reduce these degradations, several approaches could be suggested such as electrode stabilization through surface coatings or the development of functional separators capable of trapping transition metal ions. Consequently, this study provides a substantial foundation for the design of optimized materials and the elucidation of cell aging mechanisms.

Data availability

The data that support the findings of this study are available from the corresponding authors upon request.

Author contributions

Conceptualization, methodology, formal analysis, writing, review and editing, S. C.; formal analysis, writing, review and editing, A. B.; support, M. M.; support, A. F.; formal analysis, S. B.; support, J. H.; support, project administration, C. V.; supervision, F. S.; supervision, project administration, M. B.; supervision, project administration, P. S.; supervision, project administration, writing, review and editing, U. M.

Conflicts of interest

There are no conflicts to declare.

Acknowledgements

The authors would like to acknowledge the financial support provided by the European Regional Development Fund (ERDF) and the Région Hauts-de-France. The electron probe micro-analyzer (EPMA) is part of an Advanced Characterization Platform at the Chevreul Institute in Lille, France, and is supported by the ERDF. The X-ray imaging (isis4D) platform[25] has been instrumental in conducting X-Ray computed tomography experiments. The ISIS4D X-Ray CT platform has been funded by the International Campus on Safety and Intermodality in Transportation (CISIT), the Hauts de France Region, the European Community, and the National Center for Scientific Research. The authors express their gratitude to Dr David Troadec from the IEMN institute (Lille) where the FIB experiments were carried out. These experiments were supported by the French RENATECH network, the CPER Hauts de France project IMITECH and the Métropole Européenne de Lille. SC would like to thank warmly Dr Orsola Baydoun for constructive feedback.

Notes and references

1 M. Li, X. Liu, J. Wu, X. Dong, Y. Wang and S. Passerini, *Adv. Energy Mater.*, 2025, **15**, 2404037.
2 F. M. N. U. Khan, M. G. Rasul, A. S. M. Sayem and N. K. Mandal, *J. Energy Storage*, 2023, **71**, 108033.
3 C. Lan, J. Xu, Y. Qiao and Y. Ma, *Appl. Therm. Eng.*, 2016, **101**, 284–292.
4 N. E. Galushkin, N. N. Yazvinskaya and D. N. Galushkin, *J. Electrochem. Soc.*, 2018, **165**, A1303–A1308.
5 S. Chowdhury, S. Jana, S. Klayatskaya and M. Ruben, *J. Porphyr. Phthalocyanines*, 2024, **28**, 253–259.
6 S. Chowdhury, S. Jana, S. P. K. Panguluri, W. Wenzel, S. Klayatskaya and M. Ruben, *ChemSusChem*, 2024, **17**, e202301903.
7 S. Chowdhury, N. Sabi, R. C. Rojano, N. Le Breton, A. K. Boudalis, S. Klayatskaya, S. Dsoke and M. Ruben, *Batteries Supercaps*, 2024, **7**, e202300285.
8 R. I Made, J. Lin, J. Zhang, Y. Zhang, L. C. H. Moh, Z. Liu, N. Ding, S. Y. Chiam, E. Khoo, X. Yin and G. W. Zheng, *iScience*, 2024, **27**, 109416.
9 F. H. Gandoman, J. Jaguemont, S. Goutam, R. Gopalakrishnan, Y. Firouz, T. Kalogiannis, N. Omar and J. Van Mierlo, *Appl. Energy*, 2019, **251**, 113343.
10 Z. Liao, S. Zhang, K. Li, G. Zhang and T. G. Habetler, *J. Power Sources*, 2019, **436**, 226879.
11 X. Feng, S. Zheng, D. Ren, X. He, L. Wang, H. Cui, X. Liu, C. Jin, F. Zhang, C. Xu, H. Hsu, S. Gao, T. Chen, Y. Li,

T. Wang, H. Wang, M. Li and M. Ouyang, *Appl. Energy*, 2019, **246**, 53–64.
12 S. Mallick and D. Gayen, *J. Energy Storage*, 2023, **62**, 106894.
13 X. Zhou, Z. Wang, B. Sun, W. Zhang, C. Zhang, Q. Huang, S. Wang, X. Yang and H. Gong, *J. Energy Storage*, 2024, **86**, 111070.
14 A. Abaza, S. Ferrari, H. K. Wong, C. Lyness, A. Moore, J. Weaving, M. Blanco-Martin, R. Dashwood and R. Bhagat, *J. Energy Storage*, 2018, **16**, 211–217.
15 L. Huang, L. Liu, L. Lu, X. Feng, X. Han, W. Li, M. Zhang, D. Li, X. Liu, D. U. Sauer and M. Ouyang, *Int. J. Energy Res.*, 2021, **45**, 15797–15831.
16 B. Zhang, Z. Chen, Q. Tao, M. Jiao, P. Li and N. Zhou, *J. Energy Storage*, 2024, **99**, 113239.
17 J. Grabow, J. Klink, N. Orazov, R. Benger, I. Hauer and H. P. Beck, *Batteries*, 2023, **9**(10), 496.
18 S. Huang, X. Du, M. Richter, J. Ford, G. M. Cavalheiro, Z. Du, R. T. White and G. Zhang, *J. Electrochem. Soc.*, 2020, **167**, 090526.
19 R. Zhao, J. Liu and J. Gu, *Appl. Energy*, 2016, **173**, 29–39.
20 L. Greve and C. Fehrenbach, *J. Power Sources*, 2012, **214**, 377–385.
21 M. Sheikh, M. Elmarakbi, S. Rehman and A. Elmarakbi, *J. Electrochem. Soc.*, 2021, **168**, 030526.
22 S. Ge, T. Sasaki, N. Gupta, K. Qin, R. S. Longchamps, K. Aotani, Y. Aihara and C.-Y. Wang, *ACS Energy Lett.*, 2024, **9**, 5747–5755.
23 R. Xiong, S. Ma, H. Li, F. Sun and J. Li, *iScience*, 2020, **23**, 101010.
24 F. Larsson and B.-E. Mellander, *J. Electrochem. Soc.*, 2014, **161**, A1611–A1617.
25 N. Limodin, T. Rougelot and J. Hosdez, *Isis4d: in situ innovative set-ups. Plateforme d'imagerie par rayons X*, **https://isis4d.univ-lille.fr/**, accessed 22 April 2025.
26 L. Wildfeuer, N. Wassiliadis, A. Karger, F. Bauer and M. Lienkamp, *J. Energy Storage*, 2022, **48**, 103909.
27 S. Baazouzi, N. Feistel, J. Wanner, I. Landwehr, A. Fill and K. P. Birke, *Batteries*, 2023, **9**, 309.
28 T. Waldmann, S. Gorse, T. Samtleben, G. Schneider, V. Knoblauch and M. Wohlfahrt-Mehrens, *J. Electrochem. Soc.*, 2014, **161**, A1742–A1747.
29 M. S. Hosen, P. Yadav, J. Van Mierlo and M. Berecibar, *Energies*, 2023, **16**, 1046.
30 N. Lin, Z. Jia, Z. Wang, H. Zhao, G. Ai, X. Song, Y. Bai, V. Battaglia, C. Sun, J. Qiao, K. Wu and G. Liu, *J. Power Sources*, 2017, **365**, 235–239.
31 S. S. Madani, Y. Shabeer, F. Allard, M. Fowler, C. Ziebert, Z. Wang, S. Panchal, H. Chaoui, S. Mekhilef, S. X. Dou, K. See and K. Khalilpour, *Batteries*, 2025, **11**, 127.
32 B. Wang, F. L. Zhang, X. A. Zhou, P. Wang, J. Wang, H. Ding, H. Dong, W. B. Liang, N. S. Zhang and S. Y. Li, *J. Mater. Chem. A*, 2021, **9**, 13540–13551.
33 H. Oubaha, L. Fkhar, R. Cloots, F. Boschini and A. Mahmoud, *ACS Sustainable Resour. Manage.*, 2024, **1**, 1791–1801.
34 Q. Q. Qiu, Z. Shadike, Q. C. Wang, X. Y. Yue, X. L. Li, S. S. Yuan, F. Fang, X. J. Wu, A. Hunt, I. Waluyo, S. M. Bak, X. Q. Yang and Y. N. Zhou, *ACS Appl. Mater. Interfaces*, 2019, **11**, 23213–23221.
35 X. Zhang, W. J. Jiang, A. Mauger, Q. Lu, F. Gendron and C. M. Julien, *J. Power Sources*, 2010, **195**, 1292–1301.
36 C. S. Yudha, A. P. Hutama, M. Rahmawati, M. Arinawati, H. K. K. Aliwarga, H. Widiyandari and A. Purwanto, *Open Eng.*, 2022, **12**, 501–510.
37 W. Ge, Y. Fu, X. Ma, X. Li and G. Peng, *Energy Adv.*, 2022, **1**, 28–37.
38 S. H. Lee, S. Lee, B. S. Jin and H. S. Kim, *Sci. Rep.*, 2019, **9**(1), 1–7.
39 U. H. Kim, G. T. Park, B. K. Son, G. W. Nam, J. Liu, L. Y. Kuo, P. Kaghazchi, C. S. Yoon and Y. K. Sun, *Nat. Energy*, 2020, **5**(11), 860–869.
40 J. Wang, Y. Nie, C. Miao, Y. Tan, M. Wen and W. Xiao, *J. Colloid Interface Sci.*, 2021, **601**, 853–862.
41 J. Li and A. Manthiram, *Adv. Energy Mater.*, 2019, **9**, 1902731.
42 D. W. Jun, C. S. Yoon, U. H. Kim and Y. K. Sun, *Chem. Mater.*, 2017, **29**, 5048–5052.
43 M. Broussely, P. Biensan, F. Bonhomme, P. Blanchard, S. Herreyre, K. Nechev and R. J. Staniewicz, *J. Power Sources*, 2005, **146**, 90–96.
44 P. Keil, S. F. Schuster, J. Wilhelm, J. Travi, A. Hauser, R. C. Karl and A. Jossen, *J. Electrochem. Soc.*, 2016, **163**, A1872.
45 J. Park, S. S. Park and Y. S. Won, *Electrochim. Acta*, 2013, **107**, 467–472.
46 P. Serp and B. Machado, *Nanostructured Carbon Materials for Catalysis*, Royal Society of Chemistry, Catalysis Series, 2015, pp. 46–66.
47 P. Svens, R. Eriksson, J. Hansson, M. Behm, T. Gustafsson and G. Lindbergh, *J. Power Sources*, 2014, **270**, 131–141.
48 C. F. Holder and R. E. Schaak, *ACS Nano*, 2019, **13**, 7359–7365.
49 S. Bhattacharya and A. T. Alpas, *Carbon*, 2012, **50**, 5359–5371.
50 M. Zakeri, E. Abouzari-lotf, M. Miyake, S. Mehdipour-Ataei and K. Shameli, *Arab. J. Chem.*, 2019, **12**, 188–197.